Engineered Nanostructures of Antigen Provide an Effective Means for Regulating Mast Cell Activation

Zhao Deng[1], **I-Chun Weng**[2,3], **Jie-Ren Li**[1], **Huan-Yuan Chen**[2,3], **Fu-Tong Liu**[2,3,*], and **Gang-yu Liu**[1,*]

[1]Department of Chemistry, University of California, Davis, CA 95616

[2]Department of Dermatology, School of Medicine, Sacramento, University of California at Davis, CA 95817

[3]Institute of Biomedical Sciences, Academia Sinica, Taiwan, ROC

Abstract

Nanostructures containing 2,4-Dinitrophenyl (DNP) as antigen were designed and produced to investigate antibody-mediated activation of mast cells. The design consists of nanogrids of DNP termini inlaid in alkanethiol self-assembled monolayers (SAMs). Using scanning probe-based nanografting, nanometer precision was attained for designed geometry, size and periodicity. Rat basophilic leukemia (RBL) cells exhibited high sensitivity to the geometry and local environment of DNP presented on these nanostructures. The impact included cellular adherence, spreading, membrane morphology, cytoskeleton structure, and activation. The highest level of spreading and activation was induced by nanogrids of 17 nm line width and 40 nm periodicity, with DNP haptens 1.4 nm above the surroundings. The high efficacy is attributed to two main factors. First, DNP sites in the nanostructure are highly accessible by anti-DNP-IgE during recognition. Second, the arrangement or geometry of DNP termini in nanostructures promotes clustering of FcεRI receptors that are pre-linked to IgE. The clustering effectively initiates Lyn-mediated signaling cascades, ultimately leading to the degranulation of RBL cells. This work demonstrates an important concept, that nanostructures of ligands provide new and effective cues for directing cellular signaling processes.

Keywords

atomic force microscopy; engineered nanostructures; self-assembled monolayers; mast cells; antibody-mediated activation; nanografting

Mast cells are derived from bone marrow cells and are matured in tissues under the influence of stem cell factor (SCF). They can be identified by metachromatic stain or staining of tryptase. Mast cells (MC) are a major cell type involved in a number of pathological processes, from local cutaneous reactions to systemic inflammatory responses.[1–4] Mast cells express high-affinity IgE receptor (FcεRI) on the cell surface which can sensitize mast cells upon IgE binding. IgE-bound Mast cells can then be activated when encountering the antigens to which the bound IgE are specific, resulting in a signaling cascade, rearrangement of actin cytoskeleton, and a fusion of performed granule to membrane called degranulation.[1–4] Cellular activation results in production of cytokines, chemokines and growth factors, and degranulation results in release of performed mediators

---
[*]Author to whom correspondence should be addressed: Phone: (530) 754-9678: Fax: (530) 754-8557 liu@chem.ucdavis.edu.

such as histamines, beta-hexosaminidase, prostaglandins and leukotrienes. The released mediators result in characteristic symptoms of an allergic reaction.

In-depth investigations of the activation of mast cells by using model cell lines, such as bone marrow derived mast cell (BMMC) and rat basophilic leukemia (RBL), have significantly advanced our knowledge of FcεRI receptor-mediated cellular signaling processes.[1–4] Briefly, activation of mast cells can be initiated by crosslinking of FcεRI-bound, antigen-specific immunoglobulin E (IgE) using multivalent antigens. This triggers the phosphorylation of cytoplasmic immunoreceptor tyrosine-based activation motif (ITAM) *via* the Src family kinase, Lyn, causing further recruitment and activation of other kinases and substrates.[3,5] After a series of downstream signaling cascades, the antigen-IgE-receptor signaling eventually leads to mediator release through degranulation.[1]

In order to regulate mast cell degranulation much effort has been devoted to synthetic antigen analogues for the crosslinking of FcεRI receptors sensitized with IgE antibodies, as discussed in recent reviews.[6–8] Various antigen mimetics have been explored including multivalent protein conjugates such as 2,4-dinitrophenylated bovine serum albumen (DNP-BSA),[9] self-assembled monolayers (SAMs) tailored with DNP termini,[7] flexible bivalent ligands connected *via* polymer chains,[10] and bivalent and multivalent ligands connected by relatively rigid spacers, such as double strand DNA.[11,12] Among these, trivalent ligands with double strand DNA spacers exhibit the most effective stimulation for degranulation responses, and exert variable potency depending on the spacer length.[11] This high effectiveness and spacer length dependency can be rationalized by a critical Lyn-involved transphosphorylation step, which requires adequate orientation and proximity, typically nanometers, among cross-linked FcεRI.[13] Specifically, the Lyn kinase binds to the ITAM of a receptor in a cross-linked complex and then amplifies the signaling by phosphorylating the other receptor located within approximately 10 nm due to cross-linking.[2,14] We infer, from these previous studies, that the needs of polyvalent ligands separated by rigid spacer with desired length are due to the required spatial and time accessibility to the adjacent FcεRI beta chain by Lyn.

Utilizing knowledge of the activation mechanism above, engineered nanostructures of DNP haptens should, in principle, provide new and effective mimetics of polyvalent antigens. The present study takes advantage of the current advances in nanotechnology to produce complex nanostructures with designated chemical functionalities to match required spatial arrangement and accessibility. In this work, we have introduced our newly developed method that combines micromachining with atomic force microscopy (AFM) based nanografting[15,16] to produce nanostructures terminated with DNP functional groups. These engineered nanostructures have an intrinsic advantage over prior approaches due to the precise control of ligand presentation, such as geometry and local surface environment at the molecular level. As revealed in this work, this advantage is manifested in high efficiency antibody recognition and receptor clustering, and therefore, superior efficacy in cellular activation. These engineered nanostructures provide a complementary alternative to molecular mimetics reported previously, and further, have high potential for molecular level control over antigen presentation in the context of regulating specific cellular signaling processes.

RESULTS AND DISCUSSIONS

Production of Hierarchical Micro- and Nano-structures of DNP Haptens

We utilized micromachining to produce an array of micro frames, within which designed nanostructures of DNP haptens (referred to as DNP nanostructures) were created *via* AFM-based nanografting. The key fabrication steps are illustrated in Figure 1A and detailed in the

experimental section. These micro frames are clearly visible under an optical microscope, as shown in Figure 1B, and are utilized to define the position on the surface to perform nanolithography within designated frames.[17] After cleaning, the top surface is coated with 30 nm gold thin film by transferring the thermally evaporated thin film from mica, and subsequently soaked in the octadecane thiol (C18) solution to form a SAM layer which serves as the matrix for nanografting. As 30 nm gold is optically transparent,[18] we selected micro frames, *e.g.*, those labeled as P1–P4 in Figure 1B, and positioned AFM probes for nanografting as illustrated in Figure 1A.[17] For this investigation, the active component used in nanografting are thiols terminated by DNP, that is, [DNPNH(CH$_2$)$_5$COO(CH$_2$CH$_2$O)$_4$CO(CH$_2$)$_{15}$S]$_2$, abbreviated as DNP-thiol.

In the areas of P1–P4, four different nanostructure patterns are produced, each in duplication. These patterns were characterized *via* AFM as shown in Figure 1C,[17] and important geometric parameters are summarized in Table I. The total size of each nanostructure pattern is 80 μm × 80 μm, covering most areas defined by the micro frame. The backbone of the DNP-thiol is longer than that of C18 and the termini are more hydrophilic than methyl, thus the DNP nanostructures exhibit higher contrast than the surrounding C18 matrix in both topographic and lateral force images (shown in Figure 1C).[17] The four series of nanostructure patterns shown in Figure 1C are designed to explore the impact of geometry on the response of RBL cells.[17] In nanostructure P1, the pattern is double lined nanogrids, with designed periodicity of 305 ± 5 nm (the distance between repeated unit cells). The line width, defined at the FWHM (full width at half maximum) from their AFM topograph, is 9.4 ± 1.0 nm. The nearest neighbor lines are separated by 98 ± 4 nm from edge to edge. The two P2 patterns have the same geometry as P1 with the periodicity of 147 ± 6 nm, as also quantified in Table I. DNP nanostructures in P3 and P4 consist of single lined nanogrids. The lines are wider than those of P1 and P2, with the width of 19.3 ± 2.5 and 17.1 ± 1.7 nm in P3 and P4, respectively. The periodicity of P3 and P4 are 81 ± 5 and 39 ± 4 nm, respectively. The DNP coverage of P1, P2, P3 and P4 are $18 \pm 2\%$, $34 \pm 3\%$, $49 \pm 3\%$ and $54 \pm 2\%$, respectively. As will be demonstrated later in this paper, DNP haptens engineered in P4 induced the most potent stimulation for RBL cells.

Engineered Nanostructures Impact Significantly the Adherence, Spreading, and Activation of Mast Cells

Exposing RBL cells to the engineered structures after sensitization[19] with anti-DNP IgE allowed the investigation of the cellular responses to these surface bound antigens. As shown in the bright-field optical micrograph in Figure 2B, significantly different responses of RBL cells were clearly visible, when compared among nanostructures. First, the number of adhered cells increased from P1 to P4: 4, 4, 16 and 19, respectively. This trend and number of cells were highly reproducible among all three independent experiments using the same design of engineered nanostructures. We further compared fabricated nanostructure patterns with SAMs composed of pure DNP-thiols, and found P4 exhibited almost the same RBL coverage (8.5 cells per 80 × 80 μm^2) as the pure DNP SAMs (8.0 cells per 80 × 80 μm^2), despite the higher surface concentration of antigens on the pure SAMs.

Second, the activation potency, as indicated by the percentage of activated cells among adhered cells, was sensitive to the presentation of DNP at the nanometer level. The identification of activated cells was based on prior knowledge that activation of mast cells exhibits a characteristic morphology of membrane ridges/ruffles,[9,20,21] with the underlying F-actin rearranging from a relatively homogeneous distribution to a heterogeneous network.[22,23] In this investigation, the membrane morphology was imaged using AFM on hydrated cells after 1 hour incubation on surface antigens. After the completion of the AFM study, the cytoskeletal F-actin distribution was labeled *in situ* and visualized using confocal imaging following the known protocol of fluorophore-conjugated phalloidin assay.[23] The

one hour incubation time was to ensure the capture of dramatic morphological changes at the membranes before the granule regeneration process, which could take a couple of days.[24] The characteristic cellular structures from our combined AFM/confocal microscopy study are shown in Figure 2 (middle and right columns), in which the activated cells can be easily identified. Taking the left frame of P4 nanostructures (Figure 2A) as an example there were a total of 9 cells within the confinement of the micro-frame. Among them, the AFM topographic image shown in Figure $2E_4$ indicates that 6 cells exhibited membrane ridges (the well-spread cell in mid-top), while the corresponding confocal image in Figure $2E_4'$ revealed a very heterogeneous network of F-actin on these cells.[17] As a result, the activation efficiency was quantified as 66.7% (= 6/9) in this specific case. Following the same protocol, from all three experimental groups involving engineered nanostructures, the activation efficiency on C18 SAMs and P1 were both less than 15% which could be considered as background activation for RBL systems, *i.e.* RBL cells could self-activate without external stimuli. The results for other nanostructures, P2, P3 and P4, were 54 ± 11%, 64 ± 4%, and 69 ± 6%, respectively. By the well-known student-T test, the results indicated that there is no similarity between P2 and P3 with t = 4.7 and the statistical difference is 99.999% ($\alpha = 8.3 \times 10^{-7}$). For P3 and P4, t = 4.3, the statistical difference is 99.998% ($\alpha = 2.2 \times 10^{-6}$). Therefore, we can conclude with more than 99.999% confidence that they are different, and follow the sequence of P1<P2<P3<P4. This high confidence should be considered solid by any standard of statistics among *in vitro* studies. These observations reveal the multiple functions of AFM: cell count, activation assessment, and high resolution structure characterization *in vitro*.[21]

To further compare the activation efficacy of engineered nanostructures in a proper context, we quantified the activation percentage for all nanostructures in comparison with pure DNP SAMs and mixed SAMs with the solution ratio of DNP:C18 = 1:1, as well as DNP-BSA coated on coverslips. Both DNP presenting SAMs and surface-coating DNP-BSA have been used previously as antigen.[7,9] The averaged percentages of activated cells on examined antigen-presenting surfaces from all experimental groups under the same conditions are presented in Figure 3. Total numbers of cells examined were 143, 107, 70 and 57 for DNP-BSA layers, pure C18 SAMs, mixed SAMs, and pure DNP SAMs, respectively. The cell counts are 20, 15, 35 and 51 for nanostructures of P1, P2, P3, and P4, respectively. Among SAM-based systems, P3 and P4 compared more favorably to all others, including the pure DNP SAMs, despite their lower DNP surface coverage. In addition, P3 and P4 both exhibited higher activation potency than DNP-BSA layers. The fact that nanostructures stimulated mast cells more effectively than the pure DNP SAMs and DNP-BSA layers unambiguously demonstrates that the high efficacy is not due to the higher surface antigen concentration. We therefore infer that the local structure of antigen is critical. Important structural parameters in the nanostructure pattern P4 include: (a) nanogrids of DNP haptens; (b) line width and edge-to-edge separation among DNP nanolines of 17.1 ± 1.7 and 22 ± 5 nm, respectively; and (c) the apparent height of DNP lines being 1.4 ± 0.3 nm.

Third, AFM topographic images can be used to indicate the extent of activation. Taking advantage of the high spatial resolution and accuracy in height measurement, AFM enables imaging of the lateral and vertical dimensions of RBL cells as well as membrane ridges on those cells which are activated. From prior SEM studies, it is well known that the activation of mast cells is manifested in the transition of membrane morphology from homogeneous villi to heterogeneous ridges.[9,20,25] Taking advantage of the 3D information revealed by AFM, the threshold of ridges versus villi among RBL cells are 3 μm long, with an apparent height of 0.5 μm.[22] The degree of activation pertains to the number or density of membrane ridges as demonstrated previously using the combined AFM and confocal microscopy investigations.[22] The F-actin reorganization is characteristic of the RBL activation as revealed by previous confocal imaging.[9,21,22,26] The membrane ridges observed in AFM

images are attributed to the morphology of lipid bilayer covering the F-actin network underneath.[22] With this criterion, RBL cells on the nanostructure pattern P4 exhibited the highest degree of activation. Taking the cell located in the upper middle region in Figure $2E_4$ as an example, 19 ridges were visible on the cortical membrane with the length measured from 3.3 to 9.7 μm, and height measured from 0.5 to 0.7 μm. The distribution of these membrane ridges matched exactly the pattern of F-actin as seen from the corresponding confocal microscopic image (Figure $2E_4'$). The numbers of membrane ridges for other nanostructures are 0, 0, 7 and 9 for P0, P1, P2 and P3 patterns, respectively. In comparison to P4, RBL cells on other antigen-presenting surfaces possessed fewer and less protrusive membrane ridges.

Finally, the impact of nanostructures on the formation and alignment of actin clusters on the ventral membrane, *i.e.*, the membrane facing the substrate, as well as the pertaining cellular locomotion were also investigated. As shown in Figure 4, the cross-sectional confocal images taken at the interface between the ventral membrane of RBL cells and nanostructures revealed a large number of actin clusters (bright spots) on P3 and P4, whereas the amount of these clusters on C18 controls (P0) and P1 was significantly lower.[17] Among all four types of nanostructures (inserts in Figure 4), the highest number of actin clusters was observed on P4, where a total of 232 actin clusters were counted within the two micro-frames. The least number of actin clusters was observed for RBL cells on C18 SAMs, where only 33 actin clusters were observed on the 15 cells within the entire micro-fabricated area (17 frames). In addition, a visible degree of actin cluster alignment was observed on nanostructures, as highlighted by yellow lines in Figure 4.[17] Specifically, in the case of P4 there were at least three groups of actin clusters aligned vertically, and two groups of actin clusters aligned horizontally, following the two main axes of the nanogrids. These actin clusters formed at the interface, as identified from previous microscopic investigations, might lead to formation of podosomes[27] which were observed for RBL cells adhered to substrates.[28–30] Since actin clusters are implicated in podosome formation and associated with cell locomotion,[28] nanostructures of DNP could provide an alternative means to guide cellular movement and spreading.

The impact on locomotion can also be seen from the cell spreading: with the highest cell spreading observed on P4, followed by P3, P2, and then P1 and C18. Between P1 and C18, there was no significant difference in cellular morphology observed, due to the low biocompatibility of methyl termini and lack of activation (Figure $2E_0$, $2E_1$).[17] For a fair comparison (to de-convolute the impact from cell population on the cell spreading), in each category we picked the cell with the highest spreading and quantified the spreading area using the AFM images. The measured quantities were 561.9, 608.9, 813.5, 867.0 and 1297.3 μm^2 for C18, P1, P2, P3 and P4, respectively. This observation again indicates that the binding between DNP and IgE sensitized RBL plays a key role in subsequent cellular motion. It also clearly demonstrates that the distribution of the antigens at the molecular level impacts the arrangement of cytoskeletal components, and leads to variations in locomotion and spreading.

Rationalization of the Observed High Activation Efficacy of Nanostructures

Since the activation efficiency in RBL cells strongly correlates to the antigen-presenting platform as shown above, the local structure of DNP haptens on a surface must play a crucial role in regulating the IgE-FcεRI clustering as well as the subsequent downstream signaling cascades. High-resolution AFM images of various forms of DNP presentations, including nanostructures, pure and mixed C18-DNP SAMs, and the control C18 SAMs, were taken and shown in Figure 5.[17] The AFM topographs clearly revealed the structural differences of these ligand-presenting surfaces at near molecular level, as shown in Figure 5E–H.[17] Note that the images in Figure 5E–H represent characteristic structures of these

systems as we have imaged at least ten representative areas for each sample, and at least three samples were tested for each presentation.[17] *The AFM topograph of C18 SAMs is shown in* Figure 5E, where bright features correspond to closely-packed alkanethiols of several nanometers in lateral *dimension. These domains are surrounded by dark areas or domain boundaries and other defects such as etch pits.* This structure of C18 SAMs observed is consistent with prior reports,[31,32,33] and the rms roughness measures 0.2 nm. This well-ordered SAMs with methyl termini provides a good baseline reference for the comparative study. Mixed C18-DNP SAMs as exemplified in Figure 5F exhibited phase segregation, that is, presented tall DNP domains (bright) and short C18 regions (dark).[17] The phase segregation behavior is characteristic of binary SAMs.[34–37] Typical domain size of DNP in the mixed SAMs is 9.6 ± 5.8 nm, with the center-to-center separation ranging from 10.7 to 32.5 nm and the edge-to-edge separation from 5.6 to 23.6 nm. The DNP domains were 0.3 ± 0.1 nm above the surrounding C18 matrix. The surface coverage of DNP domains measured $35 \pm 5\%$ based on analysis of topography and lateral force images. Pure DNP SAMs also exhibited lateral heterogeneity. The bright contrast represents more densely packed DNP molecules, whose lateral dimension measures 6.7 ± 2.9 nm. However, unlike the mixed C18-DNP SAMs where high DNP domains are segregated by their C18 surroundings, the DNP domains were mostly connected, as shown in Figure 5G, with the surrounding being less densely packed DNP molecules.[17] The DNP domains had apparent height of 0.5 ± 0.2 nm above surrounding molecules. For DNP nanostructures P4 shown in Figure 5H, the DNP nanogrids were 1.4 ± 0.3 nm taller than the surrounding C18 SAMs. The average line width was 17.1 ± 1.7 nm and the edge-to-edge separation was 22 ± 5 nm among nearest neighbor lines. The surface coverage of DNP-thiol molecules on P4 was $54 \pm 2\%$.

One would expect different immobilization behavior if exposing the surface to IgE in solution because conceptually, ligand presentation at a molecular or nanometer level significantly impacts the subsequent biochemical reaction.[38,39] Previous observations indicated that protein binds to surface ligands more effectively *via* long and flexible polymer tethers than short and rigid ones.[40,41] Sufficient length and flexibility afford the ligand to match the protein binding site.[42–44] In fact, DNP haptens with intermediate chain lengths of $1.1 – 1.3$ nm exhibited the most potent binding to an antibody.[45,46] Flatter systems of synthetic lipid bilayers containing DNP haptens as surface ligands are more flexible, but high flexibility does not mean high recognition by antibody. Adequate flexibility is required in antibody-antigen recognition. For specific and stable antibody-antigen recognition, divalent bindings between the two Fab domains and antigens (DNP termini) underneath are preferred, as illustrated in Figure 6A. The DNP termini in P4 exhibited the highest apparent height, 1.4 nm above the surrounding region. AFM height is a collective measure of density and packing of DNP ligands, and also a measure of the mechanical flexibility of the ligand. Technology of AFM-based nanografting enables tuning flexibility to match antibody-antigen recognition. Since only one DNP molecule can enter a Fab binding pocket of an antibody, DNP molecules at the edges of nanolines have sufficient flexibility to reach the two binding sites at the Fab domains of IgE. Therefore, among all investigated antigen-presenting platforms, DNP nanogrids P4 provide the most favored binding to IgE due to the following intrinsic advantages: (a) flexibility and high exposure of DNP domains at the edges of nanografted patterns; (b) less steric hindrance of taller DNP domains for antibody-antigen recognition; (c) well-defined edge-to-edge separation to match the spatial requirements for the IgE-FcεRI dimer and cluster formation.

In this cellular study, IgE molecules are located at the membrane surface of RBL cells following sensitization. Since the presentation of DNP leads to a different binding situation with IgE molecules, as discussed above, the recognition events likely result in variations in receptor clusterization, as each IgE is linked with an FcεRI receptor at the cellular

membrane. As described in the introduction, forming basic activation dimers and clusters fulfills the critical spatial requirement for subsequent protein binding, such as Lyn and Syk, and downstream activation.[47, 48] Separation between adjacent IgE-FcεRI complexes is estimated to be around 20 nm in the dimers or clusters, as illustrated in Figure 6B. This estimation is based on the size of the IgE-FcεRI complex[49–51] including recruited Syk[52] and Lyn[53], and is reasonable according to the crystal structure and corresponding mass weighted volume of those recruited proteins (IgE, 190kDa; FceRI$_{αβγ2}$, 76kDa; LYN, 56kDa; SYK, 72kDa) that compose the IgE-FcεRI complex.[49–55] Using simple statistical analysis, we can compare the probability to form dimers and clusters among the antigen-presenting surfaces by selecting a typical DNP domain first, and then draw a circle of a 20 nm radius around this typical binding site. If the circle hits another DNP domain, there is likely an adjacent IgE-FcεRI complex, due to the high affinity of DNP to anti-DNP IgE.[38] If this rational remains valid, we project that the optimal design should be the presentation shown as the insert in Figure 6B, where DNP nanodots are arranged in hexagonal arrays with 20 nm periodicity, although we fully recognize that the actual situation could be more complex than offered by simple statistical analysis. Three examples are given in Figure 6C–E, representing the scenario on the surface of mixed C18-DNP SAMs, P2 and P4. In the case of mixed SAMs (Figure 6C), while the center of DNP domain is the strongest binding site, the circles hit 2 DNP binding sites. On P2, DNP at the edge of nanolines represents the IgE binding site, and a total of 5 DNP binding sites were hit by the circle, but only 3 remain viable due to the steric hindrance (Figure 6D). As for P4 shown in Figure 6E, we selected two representative sites for this exercise (center of the two circles in Figure 6E). The two circles hit 4 and 7 sites, the initial binding site located in the middle of line or at the cross-section, respectively. However, if one edge is occupied, spatial hindrance may forbid the other edge to attract another IgE-FcεRI complex. Therefore, among 7 potential IgE-FcεRI receptor binding sites, 4 were viable, as marked by blue crosses shown in Figure 6E. DNP sites in nanogrids exhibit a higher probability of IgE binding due to the larger apparent height, and induce a higher degree of clustering due to their matching location at nanometer level. Even though the edge-to-edge separation of P4 is close to P2, the highest apparent height and the highest DNP coverage of P4 nanorods favor binding to IgE, resulting in higher activation efficiency over P2. These combined advantages lead to superior activation efficiency for nanostructure P4.

Given the length scale of signaling clusters which are in the range of nanometers, nanofabrication techniques provide an advantage of positioning membrane receptor-binding ligands with nanometer precision for regulation of specific signaling pathways. In the case of DNP nanogrids the ligand distribution, geometry, and local environment can be designed to optimize antibody binding and cluster formation. This finding could be extrapolated into generic practice such that nano-engineered structures with well-defined geometry and functionalities can serve as a platform to regulate cellular responses to stimuli and receptor-mediated cell signaling pathways, as well as downstream cellular behaviors. The exquisite spatial precision defined by AFM-based nanografting[16] enables many polyvalent processes to be investigated systematically and with molecular level control. Potential applications of these nanoarrays could include new biochips or sensors consisting of designed micro- and nano-structures of designed functionality, as well new biomaterials or scaffolds that require accurate micro and nanofabrication.

Summary

Combined micromachining and nanolithography enables hierarchical micro- and nano-structures of designed functionalities to be produced on surfaces for a wide-range of biological applications. The combination of AFM and confocal microscopy allows *in situ* structural characterization of before and after fabrication, and *in situ* monitoring of cellular

morphology and intracellular structure upon exposure of nanostructures to cells. The specific nanostructures produced contain DNP nanogrids designed for investigation of anti-DNP IgE-mediated activation of mast cells. Nanometer precision is attained using nanografting. RBL cells exhibited high sensitivity to the geometry and local environment of DNP presented on these nanostructures. The impact includes cellular adherence, spreading, membrane morphology, cytoskeleton structure, and activation. The highest level of spreading, and activation was induced on nanogrids with 17 nm line width, 40 nm periodicity, with DNP haptens 1.4 nm above the surroundings. The superiority is attributed to two main factors. First, DNP termini at the edges of nanostructures are of adequate exposure and flexibility to be recognized by the IgE at the cellular membrane. Second, the arrangement of these DNP termini at nanostructures promotes clustering of FcεRI receptors. The clustering effectively initiates Lyn-mediated signaling cascades, ultimately leading to the degranulation of RBL cells. This work demonstrates the important concept that nanostructures of specific ligands provide new and effective cues for directing cellular signaling processes.

METHODS

Reagents

Octadecanethiol (abbreviated as C18) with a purity > 95% was purchased from Sigma-Aldrich and used without further purification. [DNPNH$(CH_2)_5$COO$(CH_2CH_2O)_4$CO$(CH_2)_{15}$S]$_2$, (abbreviated as DNP-thiol) with a purity of more than 95% was purchased from ProChimia (Gdansk, Poland) and used without further purification. 2-butanol was purchased from Fisher Scientific (Pittsburg, PA) and N, N-dimethylformamide (DMF) from EMD Chemicals (Gibbstown, NJ), and used as received. High quality monoclonal mouse-anti-DNP IgE (abbreviated as IgE) was attained following our protocols developed previously.[56]

Preparation of Transparent Ultra-flat Gold Films on Micro Fabricated Glass Coverslips

Step 1, a carbide scriber (Moody Tools, Inc., Warwick, RI) was used to mill the designed micro-pattern, that is, micro grids with unit side length of 120 micron, on one side of 12 mm glass coverslips (Fisher Scientific, Pittsburg, PA). The scriber was mounted on a CNC turret miller (Hardinge Inc., Elmira, NY) with a precision of 10 μm. In brief, a micron-precision miller is used to sculpture arrays of micro frames (120 μm × 120 μm each) on coverslips. The fine milling groves are approximately 10 μm in width. The micro pattern is located at the central region on the bottom surface of the cover slip. An extra line drawn on the top-right corner of the micro pattern is used to register the position of the fabricated nanostructures in the subsequent cell culture experiments. The pre-patterned coverslips were then sequentially washed by piranha solution, water and ethanol, dried in air and kept for use in step 3 as described below.

Step 2, gold (99.999%, Alfa Aesar, Ward Hill, MA) was deposited in a high-vacuum evaporator (Model DV502-A, Denton Vacuum, Moorestown, NJ) at a base pressure below 2 × 10^{-6} Torr onto freshly cleaved mica substrates (clear ruby muscovite, Mica New York Corp.) at room temperature. The typical evaporation rates were 3 Å/s, and the thickness of the gold films was controlled at 30 ± 1 nm. Immediately after removal from the chamber, the gold coated mica substrates were annealed in the H$_2$ flame for 1 min in order to obtain coalesced gold grains on the mica. Then the gold thin film on mica was cooled in air to room temperature and kept for use in step 3.

Step 3, a small droplet of epoxy glue (Epo-tek 377, Epoxy Technology, Billerica, MA) was applied to each of the dried coverslips from step 1. The coverslips were then placed on the

gold/mica substrate from step 2 with the glue attached side facing down. The glue was then cured at 150 °C overnight. After being removed from the oven, the glass coverslips with gold thin film were peeled off from the mica substrate.

Preparation of Self-Assembled Monolayers

Three types of self-assembled monolayers (SAMs), including the C18 SAM, DNP SAM and binary C18-DNP SAM, were prepared on the gold coated coverslips described in the previous section, and used as platforms for investigation of mast cell activation. C18 SAMs were prepared by immersing gold coated coverslips into a solution containing 0.02 mM C18 in secondary butanol for at least 24 hr. DNP SAMs were prepared by dissolving the DNP compound in DMF first to obtain a stock solution of 0.2 mM, and subsequently diluted with secondary butanol to reach a final concentration of 0.01 mM (DMF: second butanol = 1:19). Since each DNP disulfide molecule contains two thiol chains, the effective thiol concentration is also 0.02 mM. Gold coated coverslips were then immersed into this DNP solution for at least 24 hr to form SAMs. The binary SAM composed of C18 and DNP was prepared by first mixing C18 and DNP compounds in DMF at a 2:1 molar ratio to reach a total effective thiol concentration of 0.4 mM, and then the DMF solution was diluted by secondary butanol to reach a final concentration of 0.02 mM (DMF:2-butanol = 1:19). Gold coated coverslips were then immersed in the thiol mixture for at least 24 hr to form SAMs. The mixed solvent of 5% DMF in secondary butanol produced the best packing of DNP molecules on gold substrates, based on our investigation of the solvent dependence of the SAMs.

Preparation of DNP-BSA Coated Silicon Substrates and SEM Imaging

Thin coatings of 2,4-dinitrophenylated bovine serum albumin (DNP_{30}-BSA, abbreviated as DNP-BSA in the manuscript) were prepared by soaking an oxidized silicon substrate in PBS buffer containing 20 μg/mL protein for 1 h following previously reported protocols.[21,22,47] The immobilization is of physical adsorption in nature, as previously reported.[57–59] DNP_{30}-BSA was purchased from Invitrogen (Carlsbad, CA) and used without further purification. The substrate used for protein adsorption was Si(111) (Virginia Semiconductor Inc., Fredericksburg, VA). Before use, the Si(111) substrates were cleaned by immersion in piranha solution, which is a mixture of sulfuric acid and hydrogen peroxide (EMD Chemicals, Gibbstown, NJ) with a (v/v) ratio of 3:1. Substrates were then rinsed copiously with deionized water and dried with nitrogen. The cleaning protocols using piranha solution and copious washing exposed silicon oxide (SiO_2) often with hydroxyl termini at the surface of the wafer. These clean SiO_2 surfaces are less toxic to proteins than pure Si(111) surfaces, and allow for chemical modification such as siloxane SAMs with designated termini.

For SEM characterization, 1% osmium tetroxide (OsO_4, Sigma-Aldrich, St. Louis, MO) in deionized water was used as the secondary fixative and treated with cell samples for 30 min at room temperature. Cell samples were then dehydrated further in an ethanol/water mixture of 25%, 50%, 75%, 90%, and 100% for 10 min each. Dehydration in 100% ethanol was performed three times. Dehydrated samples were treated with hexamethyldisilazane (HMDS, Sigma-Aldrich, St. Louis, MO) for drying biological samples as previously reported.[60–62] Samples were immersed twice for 30 s in pure HMDS followed by 10 min of air-drying. The morphology of activated RBL cells was observed with a Hitachi S-800T FE-SEM (Hitachi High Technologies America, Inc., Pleasanton, CA) with the routine accelerating voltage of 2.5 kV.

Culture of RBL Cells

Rat basophilic leukemia cells (RBL-2H3, purchased from ATCC, Manassas, VA) were maintained at 37 °C and 5% CO_2 in RPMI 1640 medium (GIBCO-BRL, Grand Island, NY)

containing 10% fetal bovine serum (HyClone, Logan, UT) and supplemented with L-glutamine (GIBCO-BRL, Grand Island, NY), penicillin-streptomycin (GIBCO-BRL, Grand Island, NY), sodium pyruvate and HEPES buffer.[26] Cells were first sensitized with 0.5 μg/ml anti-DNP IgE overnight, and then washed with phosphate buffered saline (PBS, D8662, Sigma-Aldrich, St. Louis, MO) to remove excess IgE. Activation of the sensitized cells was triggered by plating them onto the SAMs and nanostructure patterns containing DNP haptens. Stimulation was terminated after 1 hr incubation by adding 3.7% formaldehyde. The 1 hr incubation time was chosen to ensure most of the cells, when activated, reached an activation stage at which dramatic morphological change would occur because it is known that activation of mast cells does not occur in a synchronized manner.[63]

AFM-based Nanografting

AFM was used for the characterization of SAMs and fabrication of DNP nanostructures. The AFM (MFP-3D-SA, Asylum Research, Santa Barbra, CA) has a scanning range of 90 μm, 90 μm, and 16 μm in X, Y, and Z directions, respectively. Each of the X, Y, Z scanners has a closed-loop configuration with the precision of 0.6 nm, 0.6 nm, and 0.3 nm, respectively. Sharpened Si_3N_4 micro levers (Veeco Metrology Group, Santa Barbara, CA) with a force constant of 0.1 N/m were used for fabrication and characterization.

In addition to high-resolution imaging of surface topography, the high scanning range and high movement precision of the Asylum AFM enable fabrication of nanostructures with a large patterning area for cellular studies, and high precision for individual antibody binding. The fabrication method used was an AFM-based nanografting technique developed by our group.[15] Briefly, a SAM layer was immersed and imaged in a solution containing a different thiol. Upon scanning by the AFM probe above the displacement threshold the matrix thiols were removed and replaced by the new absorbates in solution. In this study, C18 was used to form the matrix, whereas DNP molecules were used as the replacement molecules to construct the desired nanostructure patterns. Sharpened Si_3N_4 micro levers (Veeco Metrology Group, Santa Barbara, CA) with a force constant of 0.58 N/m were used for all nanografting experiments.

Combined AFM and Laser Scanning Confocal Microscopy for Characterization of Nanostructures and RBL Cells

A combined laser scanning confocal microscopy (LSCM) and AFM system was used to image the cells on SAMs and nanostructures. The AFM's X, Y and Z scanners have the same configurations as those described in the previous section except the stand-alone base is replaced by the stand of the LSCM (Olympus Fluoview 1000, Olympus America, Central Valley, PA). The XY scanning of LSCM was performed with a pair of galvanometric mirrors, yielding a wide scanning range that images both individual cells and cell colonies. All confocal images were acquired using a Plan Apo N (60X, N.A. = 1.42) oil immersion bright-field objective with a working distance of 0.15 mm.

The integration of AFM and LSCM was achieved by modifying the LSCM's sample stage to accommodate the AFM scanner. The AFM scanner was designed in such a way that it has a window at the center to allow the alignment of the AFM tip with the laser beam. This enables concurrent imaging of desired cells by both microscopes. An in-house constructed sample holder was utilized for simultaneous AFM and LSCM imaging in the same media.

For AFM imaging, cells were fixed with 3.7% formaldehyde for 30 min and maintained in PBS after incubation on SAMs and nanostructure patterns. Contact mode AFM was used to image the morphology of the whole cell or cell colonies. Silicon cantilevers with a spring

constant 0.03 N/m (CSC38 lever B, MikroMasch, San Jose, CA) were used, and the imaging force was controlled to be less than 1 nN, as determined by force-distance curves.

After AFM imaging, cell samples were labeled *in situ* following standard protocols of phalloidin assay from the vendor (Invitrogen). The PBS in the sample holder was replaced by 0.1% Triton-X 100 (21123, Invitrogen, Carlsbad, CA) to permeabilize the cell membrane for 5 min at room temperature. After washing twice with PBS, cells were stained with 0.1 μM of Alexa 568 phalloidin (A12380, Invitrogen, Carlsbad, CA) for 20 min. Upon washing twice with PBS again, cells were immediately imaged by the LSCM under the buffer. The LSCM images were collected between 555 and 630 nm under the excitation of 543 nm.

All AFM images of various forms of DNP presentations were acquired and analyzed using Asylum MFP3D software developed on the Igor Pro 5.04 platform. The display of AFM topographic images for cells needs to consider the range of cellular height (2–10 μm). While the 3D geometry is quantified using topographic images, deflection images (collected simultaneously with topograph) are displayed to allow clear visualization of structural features on the cell membrane in a wide dynamic range. The coverage of DNP ligands was calculated using the masking function built in the manufacturer's software, taking advantage of the clear contrast between DNP and methyl termini, in both topographic and lateral force images.

All confocal fluorescence images were acquired and analyzed using the Olympus Fluoview 1.6 software. To visualize the F-actin network beneath the cortical membrane, 3D stacking images of phalloidin were displayed using Z-projection to present the 3D spatial distribution of dye in one frame. To visualize the actin at the ventral membrane, 2D cross-sectional view was taken at the interface between the cell and substrate.

Acknowledgments

References

1. Sharma BB, Apgar JR, Liu FT. Mast Cells - Receptors, Secretagogues, and Signaling. Clin Rev Allergy Immunol. 2002; 22:119–148. [PubMed: 11975419]

2. Wilson BS, Pfeiffer JR, Oliver JM. Fc Epsilon RI Signaling Observed from the Inside of the Mast Cell Membrane. Mol Immunol. 2002; 38:1259–1268. [PubMed: 12217393]

3. Gilfillan AM, Tkaczyk C. Integrated Signalling Pathways for Mast-Cell Activation. Nat Rev Immunol. 2006; 6:218–230. [PubMed: 16470226]

4. Metcalfe DD, Baram D, Mekori YA. Mast Cells. Physiol Rev. 1997; 77:1033–1079. [PubMed: 9354811]

5. Rivera J, Gilfillan AM. Molecular Regulation of Mast Cell Activation. J Allergy Clin Immunol. 2006; 117:1214–1225. [PubMed: 16750977]

6. Huang YF, Liu HP, Xiong XL, Chen Y, Tan WH. Nanoparticle-Mediated IgE-Receptor Aggregation and Signaling in RBL Mast Cells. J Am Chem Soc. 2009; 131:17328–17334. [PubMed: 19929020]

7. Senaratne W, Sengupta P, Jakubek V, Holowka D, Ober CK, Baird B. Functionalized Surface Arrays for Spatial Targeting of Immune Cell Signaling. J Am Chem Soc. 2006; 128:5594–5595. [PubMed: 16637600]

8. Holowka D, Sil D, Torigoe C, Baird B. Insights into Immunoglobulin E Receptor Signaling from Structurally Defined Ligands. Immunol Rev. 2007; 217:269–279. [PubMed: 17498065]

9. Pfeiffer JR, Seagrave JC, Davis BH, Deanin GG, Oliver JM. Membrane and Cytoskeletal Changes Associated with IgE-Mediated Serotonin Release from Rat Basophilic Leukemia-Cells. J Cell Biol. 1985; 101:2145–2155. [PubMed: 2933414]

10. Baird EJ, Holowka D, Coates GW, Baird B. Highly Effective Poly(ethylene glycol) Architectures for Specific Inhibition of Immune Receptor Activation. Biochemistry. 2003; 42:12739–12748. [PubMed: 14596588]

11. Sil D, Lee JB, Luo D, Holowka D, Baird B. Trivalent Ligands with Rigid DNA Spacers rReveal Structural Requirements for IgE Receptor Signaling in RBL Mast Cells. ACS Chem Biol. 2007; 2:674–684. [PubMed: 18041817]

12. Paar JM, Harris NT, Holowka D, Baird B. Bivalent Ligands with Rigid Double-Stranded DNA Spacers Reveal Structural Constraints on Signaling by Fc Epsilon RI. J Immunol. 2002; 169:856–864. [PubMed: 12097389]

13. Seagrave J, Pfeiffer JR, Wofsy C, Oliver JM. Relationship of IgE Receptor Topography to Secretion in RBL-2H3 Mast Cells. J Cell Physiol. 1991; 148:139–151. [PubMed: 1830592]

14. Metzger H. The IgE-Mast Cell System as a Paradigm for the Study of Antibody Mechanisms. Immunol Rev. 1978; 41:186–199. [PubMed: 360507]

15. Xu S, Liu GY. Nanometer-Scale Fabrication by Simultaneous Nanoshaving and Molecular Self-Assembly. Langmuir. 1997; 13:127–129.

16. Liu GY, Xu S, Qian YL. Nanofabrication of Self-Assembled Monolayers Using Scanning Probe Lithography. Accounts Chem Res. 2000; 33:457–466.

17. Deng, Z. PhD Dissertation. University of California, Davis; 2009. Engineered Nanostructures for Investigation and Regulation of Mast Cell Activation.

18. Dimilla PA, Folkers JP, Biebuyck HA, Harter R, Lopez GP, Whitesides GM. Wetting and Protein Adsorption on Self-Assembled Monolayers of Alkanethiolates Supported on Transparent Films of Gold. J Am Chem Soc. 1994; 116:2225–2226.

19. Zuberi RI, Frigeri LG, Liu FT. Activation of Rat Basophilic Leukemia-Cells by Epsilon-bp, an IgE-Binding Endogenous Lectin. Cell Immunol. 1994; 156:1–12. [PubMed: 8200029]

20. Sahara N, Siraganian RP, Oliver C. Morphological-Changes Induced by the Calcium Ionophore-A23187 in Rat Basophilic Leukemia (2H3) Cells. J Histochem Cytochem. 1990; 38:975–983. [PubMed: 1693935]

21. Zink T, Deng Z, Chen H, Yu L, Liu FT, Liu GY. High-Resolution Three-Dimensional Imaging of the Rich Membrane Structures of Bone Marrow-Derived Mast Cells. Ultramicroscopy. 2008; 109:22–31. [PubMed: 18790570]

22. Deng Z, Zink T, Chen HY, Walters D, Liu FT, Liu GY. Impact of Actin Rearrangement and Degranulation on the Membrane Structure of Primary Mast Cells: A Combined Atomic Force and Laser Scanning Confocal Microscopy Investigation. Biophys J. 2009; 96:1629–1639. [PubMed: 19217878]

23. Nishida K, Yamasaki S, Ito Y, Kabu K, Hattori K, Tezuka T, Nishizumi H, Kitamura D, Goitsuka R, Geha RS, Yamamoto T, Yagi T, Hirano T. Fc Epsilon RI-Mediated Mast Cell Degranulation Requires Calcium-Independent Microtubule-Dependent Translation of Granules to the Plasma Membrane. J Cell Biol. 2005; 171:177–177.

24. Nielsen EH, Bytzer P, Clausen J, Chakravarty N. Electron Microscopic Study of the Regeneration *in vitro* of Rat Peritoneal Mast Cells after Histamine Secretion. Cell Tissue Res. 1981; 216:635–645. [PubMed: 6165480]

25. Edgar AJ, Davies GR, Anwar MA, Bennett JP. Loss of Cell surface Microvilli on Rat Basophilic Leukaemia Cells Precedes Secretion and Can Be Mimicked Using the Calmodulin Antagonist Trifluoperazine. Inflamm Res. 1997; 46:354–360. [PubMed: 9339391]

26. Zuberi RI, Frigeri LG, Liu FT. Activation of Rat Basophilic Leukemia-Cells by Epsilon-bp, an IgE-Binding Endogenous Lectin. Cell Immunol. 1994; 156:1–12. [PubMed: 8200029]

27. Linder S, Kopp P. Podosomes at a Glance. J Cell Sci. 2005; 118:2079–2082. [PubMed: 15890982]

28. Spinardi L, Marchisio PC. Podosomes as Smart Regulators of Cellular Adhesion. Eur J Cell Biol. 2006; 85:191–194. [PubMed: 16546561]

29. Suzuki T, Shoji S, Yamamoto K, Nada S, Okada M, Yamamoto T, Honda Z. Essential Roles of Lyn in Fibronectin-Mediated Filamentous Actin Sssembly and Cell Motility in Mast Cells. J Immunol. 1998; 161:3694–3701. [PubMed: 9759894]

30. Geng LP, Pfister S, Kraeft SK, Rudd CE. Adaptor FYB (Fyn-Binding Protein) Regulates Integrinmediated Adhesion and Mediator Release: Differential Involvement of the FYBSH3 Domain. Proc Natl Acad Sci U S A. 2001; 98:11527–11532. [PubMed: 11553777]

31. Yang GH, Liu GY. New Insights for Self-Assembled Monolayers of Organothiols on Au(111) Revealed by Scanning Tunneling Microscopy. J Phys Chem B. 2003; 107:8746–8759.

32. Fukuma T, Kobayashi K, Horiuchi T, Yamada H, Matsushige K. Alkanethiol Self-Assembled Monolayers on Au(111) Surfaces Investigated by Non-Contact AFM. Appl Phys A-Mater Sci Process. 2001; 72:S109–S112.

33. Yan L, Huck WTS, Whitesides GM. Self-Assembled Monolayers (SAMs) and Synthesis of Planar Micro- and Nanostructures. Polym Rev. 2004; C44:175–206.

34. Imabayashi S, Hobara D, Kakiuchi T, Knoll W. Selective Replacement of Adsorbed Alkanethiols in Phase-Separated Binary Self-Assembled Monolayers by Electrochemical Partial Desorption. Langmuir. 1997; 13:4502–4504.

35. Chen SF, Li LY, Boozer CL, Jiang SY. Controlled Chemical and Structural Properties of Mixed Self-Assembled Monolayers by Coadsorption of Symmetric and Asymmetric Disulfides on Au(111). J Phys Chem B. 2001; 105:2975–2980.

36. Bu DL, Mullen TJ, Liu GY. Regulation of Local Structure and Composition of Binary Disulfide and Thiol Self-Assembled Monolayers Using Nanografting. ACS Nano. 2010; 4:6863–6873. [PubMed: 20931979]

37. Yu JJ, Tan YH, Li X, Kuo PK, Liu GY. A Nanoengineering Approach to Regulate the Lateral Heterogeneity of Self-Assembled Monolayers. J Am Chem Soc. 2006; 128:11574–11581. [PubMed: 16939281]

38. Jung HS, Yang T, Lasagna MD, Shi JJ, Reinhart GD, Cremer PS. Impact of Hapten Presentation on Antibody Binding at Lipid Membrane Interfaces. Biophys J. 2008; 94:3094–3103. [PubMed: 18199665]

39. Jung H, Robison AD, Cremer PS. Multivalent Ligand-Receptor Binding on Supported Lipid Bilayers. J Struct Biol. 2009; 168:90–4. [PubMed: 19508894]

40. Ahlers M, Grainger DW, Herron JN, Lim K, Ringsdorf H, Salesse C. Quenching of Fluorescein-Conjugated Lipids by Antibodies. Quantitative Recognition and Binding of Lipid-Bound Haptens in Biomembrane Models, Formation of Two-Dimensional Protein Domains and Molecular Dynamics Simulations. Biophys J. 1992; 63:823–838. [PubMed: 1420916]

41. Leckband DE, Kuhl T, Wang HK, Herron J, Muller W, Ringsdorf H. 4-4-20-Anti-Fluorescyl IgG Fab' Recognition of Membrane-Bound Hapten: Direct Evidence for the Role of Protein and Interfacial Structure. Biochemistry-US. 1995; 34:11467–11478.

42. Wong JY, Kuhl TL, Israelachvili JN, Mullah N, Zalipsky S. Direct Measurement of a Tethered Ligand-Receptor Interaction Potential. Science. 1997; 275:820–822. [PubMed: 9012346]

43. Kulin S, Kishore R, Hubbard JB, Helmerson K. Real-Time Measurement of Spontaneous Antigen-Antibody Dissociation. Biophys J. 2002; 83:1965–1973. [PubMed: 12324415]

44. Longo G, Szleifer I. Ligand-Receptor Interactions in Tethered Polymer Layers. Langmuir. 2005; 21:11342–11351. [PubMed: 16285809]

45. Cooper AD, Balakrishnan K, McConnell HM. Mobile Haptens in Liposomes Stimulate Serotonin Release by Rat Basophil Leukemia-Cells in the Presence of Specific Immunoglobulin-E. J Biol Chem. 1981; 256:9379–9381. [PubMed: 7287691]

46. Kimura K, Arata Y, Yasuda T, Kinosita K, Nakanishi M. Location of Membrane-Bound Hapten with Different Length Spacers. Immunology. 1990; 69:323–328. [PubMed: 2307487]

47. Schweitzer-Stenner R, Tamir I, Pecht I. Analysis of Fc Epsilon RI-Mediated Mast Cell Stimulation by Surface-Carried Antigens. Biophys J. 1997; 72:2470–2478. [PubMed: 9168023]

48. MacGlashan D. IgE Receptor and Signal Transduction in Mast Cells and Basophils. Curr Opin Immunol. 2008; 20:717–723. [PubMed: 18822373]

49. Garman SC, Kinet JP, Jardetzky TS. Crystal Structure of the Human High-Affinity IgE Receptor. Cell. 1998; 95:951–961. [PubMed: 9875849]

50. Wan T, Beavil RL, Fabiane SM, Beavil AJ, Sohi MK, Keown M, Young RJ, Henry AJ, Owens RJ, Gould HJ, Sutton BJ. The Crystal Structure of IgE Fc Reveals an Asymmetrically Bent Conformation. Nat Immunol. 2002; 3:681–686. [PubMed: 12068291]

51. Garman SC, Wurzburg BA, Tarchevskaya SS, Kinet JP, Jardetzky TS. Structure of the Fc Fragment of Human IgE Bound to its High-Affinity Receptor Fc Epsilon RI Alpha. Nature. 2000; 406:259–266. [PubMed: 10917520]

52. Arias-Palomo E, Recuero-Checa MA, Bustelo XR, Llorca O. 3D Structure of Syk Kinase Determined by Single-Particle Electron Microscopy. BBA-Proteins Proteomics. 2007; 1774:1493–1499.

53. Williams NK, Lucet IS, Klinken SP, Ingley E, Rossjohn J. Crystal Structures of the Lyn Protein Tyrosine Kinase Domain in Its Apo- and Inhibitor-bound State. J Biol Chem. 2009; 284:284–291. [PubMed: 18984583]

54. Silverton EW, Navia MA, Davies DR. Three-Dimensional Structure of an Intact Human Immunoglobulin. Proc Natl Acad Sci U S A. 1977; 74:5140–5144. [PubMed: 270751]

55. Nakamura T, Lozano PR, Ikeda Y, Iwanaga Y, Hinek A, Minamisawa S, Cheng CF, Kobuke K, Dalton N, Takada Y, Tashiro K, Ross J Jr, Honjo T, Chien KR. Fibulin-5/DANCE is Essential for Elastogenesis *in vivo*. Nature. 2002; 415:171–5. [PubMed: 11805835]

56. Liu FT, Bohn JW, Ferry EL, Yamamoto H, Molinaro CA, Sherman LA, Klinman NR, Katz DH. Monoclonal Dinitrophenyl-Specific Murine IgE Antibody - Preparation, Isolation, and Characterization. J Immunol. 1980; 124:2728–2737. [PubMed: 7373045]

57. Haynes CA, Norde W. Structures and Stabilities of Adsorbed Proteins. J Colloid Interf Sci. 1995; 169:313–328.

58. Fernandez-Lafuente R, Armisen P, Sabuquillo P, Fernandez-Lorente G, Guisan JM. Immobilization of Lipases by Selective Adsorption on Hydrophobic Supports. Chem Phys Lipids. 1998; 93:185–197. [PubMed: 9720258]

59. Rusmini F, Zhong ZY, Feijen J. Protein Immobilization Strategies for Protein Biochips. Biomacromolecules. 2007; 8:1775–1789. [PubMed: 17444679]

60. Carr JH, Anderson RL, Favero MS. Comparison of Chemical Dehydration and Critical Point Drying for the Stabilization and Visualization of Aging Biofilm Present on Interior Surfaces of PVC Distribution Pipe. J Appl Bacteriol. 1996; 80:225–232. [PubMed: 8642017]

61. Braet F, deZanger R, Wisse E. Drying Cells for SEM, AFM and TEM by Hexamethyldisilazane: A Study on Hepatic Endothelial Cells. J Microsc. 1997; 186:84–87. [PubMed: 9159923]

62. Araujo JC, Teran FC, Oliveira RA, Nour EAA, Montenegro MAP, Campos JR, Vazoller RF. Comparison of Hexamethyidisilazane and Critical Point Drying Treatments for SEM Analysis of Anaerobic Biofilms and Granular Sludge. J Electron Microsc. 2003; 52:429–433.

63. Zou X, Block M, Lofman C, Nilsson G. IgE-Mediated Mast Cell Degranulation and Recovery Monitored by Time-Lapse Photography. J Allergy Clin Immunol. 2001; 108:116–121. [PubMed: 11447391]
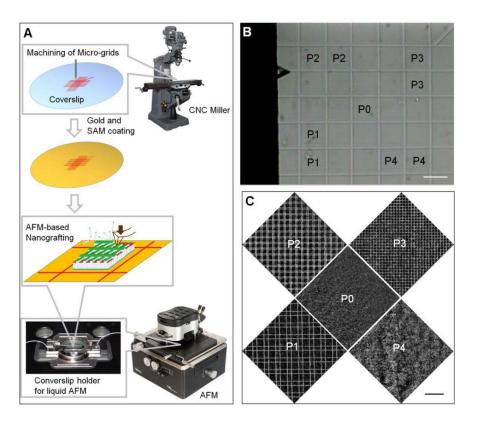
Figure 1.
[A] A schematic diagram illustrating the main steps to fabricate hierarchical micro/nano structures on gold coated coverslips. [B] A bright-field optical image showing the micro frames on the gold coated coverslip. Locations for various nanostructures are also indicated (P1–P4). [C] AFM lateral force images of the four nanostructures of DNP (P1–P4) produced by nanografting. Scale bars In [B] and [C] are 120 μm and 500 nm, respectively. Reprint from reference 17 with permission from UC Davis.
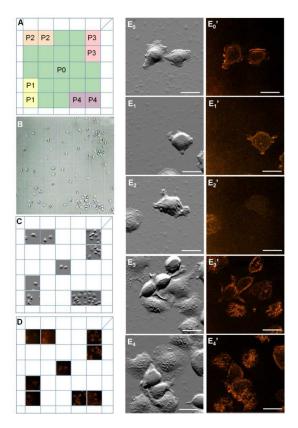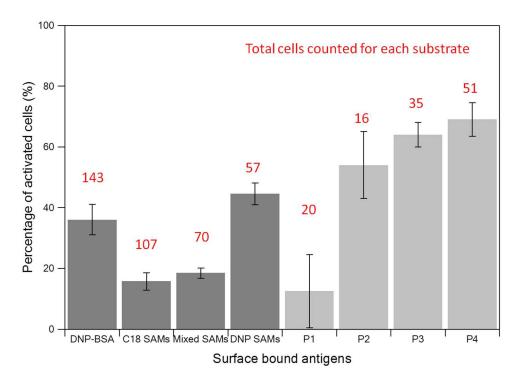
Figure 2.
[A] A schematic diagram to illustrate the design of micro/nanostructures. Locations of nanostructures P1–P4 are indicated on the design. [B] A bright-field optical image provides an overview of the surface after exposure to RBL-2H3 cells, where cell population is clearly visible. [C] Nine AFM images acquired on P1–P4 and the central matrix region (P0) to provide an overview of cellular morphology at these regions. [D] The corresponding confocal images of C. [E_0–E_4] and [E_0'–E_4'] are magnified views of the AFM and confocal images shown in C and D, respectively. Scale bars: 20 μm. Reprint from reference 17 with permission from UC Davis.

Figure 3.
Activation efficacy as a function of the geometry of DNP nanostructures (P0–P4). As a comparison, previously used presentation of DNP antigens, such as DNP-BSA layers and mixed DNP:C18 SAMs, were also measured.
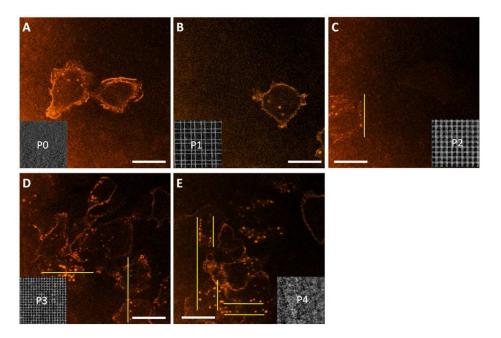
Figure 4.
Confocal images acquired at the interface between the ventral membrane and nanostructure surfaces to best capture the formation and alignment of actin clusters on [A] C18 SAM; [B] P1; [C] P2; [D] P3; and [E] P4. The yellow lines indicate examples of the aligned actin clusters as guided by the DNP nanolines underneath (inserts). Scale bars: 20 μm. Reprint from reference 17 with permission of UC Davis.
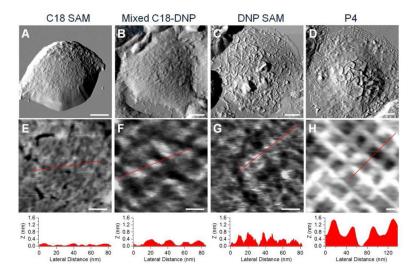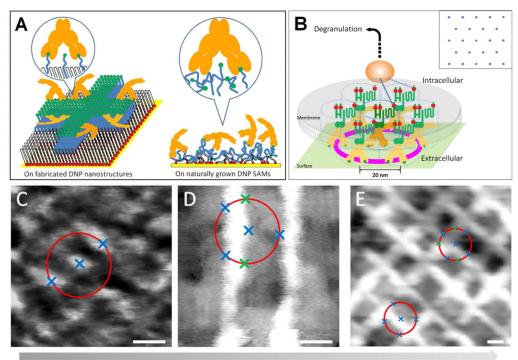
Figure 5.
Correlation of RBL intracellular structure (top row) to the molecular level packing of DNP ligands (middle row) as revealed by high-resolution AFM images. The height profile acrossing the DNP domains as marked in the AFM images is shown at the bottom row. Scale bars in [A]–[D] are 5 μm, and 20 nm in [E]–[H]. Reprint from reference 17 with permission of UC Davis.

Increasing activation potency

Figure 6.
Rationalization of the superior efficacy of nanostructures in RBL activation. [A] DNP molecules at the edges of nanstructures present favorable binding sites for IgE due to their 1.4 nm apparent height, adquate flexibility and availability for divalent binding. In comparison, pure DNP SAMs has only 0.5 nm apparent domain height, which may not enter the Fab binding pocket as effectively as the DNP nanostructures. [B] From the prospective of geometry only, the optimal arrangement of IgE-FcεRI complexes is hexagonal with 20 nm separation for the subsequent Lyn binding and downstream signaling cascade. [C]–[E] Illustrate the probability of finding activation dimer for a tyrpical IgE-FcεRI binding site (the blue cross at the center of the circle) within a mixed C18:DNP SAM, and nanostructures P2 and P4, respectively. Radius of the circle is 20 nm. Scale bars: 20 nm

Table I

Structure of DNP Domains and Their Local Environment as Characterized by AFM

	P0 (C18 SAMs)	P1	P2	P3	P4	Mixed DNP:C18 SAMs	Pure DNP SAMs
Geometry of DNP domains	N/A	double-lined grid	double-lined grid	grid	grid	nanodomains inlaid in C18 SAMs	nanodomains surrounded by defects
Periodicity (nm)	N/A	305 ± 5	147 ± 6	81 ± 5	39 ± 4	N/A	N/A
DNP line width/Domain size (nm)	N/A	9.4 ± 1.0	10.1 ± 1.9	19.3 ± 2.5	17.1 ± 1.7	9.6 ± 5.8	6.7 ± 2.9
Apparent height (nm)	N/A	1.1 ± 0.2	1.1 ± 0.2	1.3 ± 0.3	1.4 ± 0.3	0.3 ± 0.1	0.5 ± 0.2
Edge-to-edge seperation (nm,)	N/A	98 ± 4	23 ± 6	54 ± 3	22 ± 5	6 − 24	4 − 16
DNP coverage (%)	0	18 ± 2	34 ± 3	49 ± 3	54 ± 2	35 ± 5	61 ± 4